PNAS
www.pnas.org

Supplementary Information for

I_{Ks} ion-channel pore conductance can result from individual voltage sensor movements

Maartje Westhoff, Jodene Eldstrom, Christopher I. Murray, Emely Thompson and David Fedida

Corresponding Author: David Fedida
Email: david.fedida@ubc.ca

This PDF file includes:

Supplementary text for 'Materials and Methods'
Figs. S1 to S13
Tables S1 to S4

www.pnas.org/cgi/doi/10.1073/pnas.1811623116

Supplementary text for 'Materials and Methods'

Chemicals

[2-(Trimethylammonium)ethyl]methanethiosulfonate Bromide (MTSET) was obtained from Toronto Research Chemicals Inc (North York, ON, Canada). Alexa Fluor 488 C_5-maleimide was obtained from Thermo Fisher Scientific (Waltham, MA, USA). All other chemicals were obtained from Sigma-Aldrich (St. Louis, MO, USA).

Molecular Biology

The EQ, EQQ, EQQQQ constructs were generated as previously described (1). E1 was removed from EQQ and EQQQQ constructs, to produce QQ and QQQQ respectively. The E160R mutation was incorporated into the first Q1 of the fusion constructs via a gBlocks Gene Fragment (Integrated DNA Technologies, Coralville, IA, USA) with compatible restriction sites. The V319Y mutation was incorporated into the first Q1 of WT EQQ and E160R EQQ via a FragmentGENE (GENEWIZ, South Plainfield, NJ, USA) with compatible restriction sites. The tandem MTSET and fluorescence constructs were constructed by Applied Biological Materials Inc (Richmond, BC, Canada). All mutations were confirmed by sequencing. The F57W mutation was incorporated into E1 using the QuickChange II Site-Directed Mutagenesis Kit (Agilent Technologies, Santa Clara, CA, USA) via the manufacturer's protocol.

Cell Culture and Transfection

tsA201 transformed human embryonic kidney 293 (whole cell experiments) or *ltk*-mouse fibroblast cells (single channel experiments) were cultured and plated for experiments as previously described (1, 2). Cells were transfected using Lipofectamine2000 (Thermo Fisher Scientific) as per the manufacturer's protocol. The WT/E160R/F57W (E)QQ/(E)QQQQ and EQ constructs (WT/E160R/F57W EQ) were transfected with GFP in a 3:1 ratio. When co-expressed with E1-GFP (hereafter referred to as E1), the ratio was 3 E1:1 Q1 construct. Throughout the paper, the E160R mutation in Q1 is denoted by an asterisk (Q*) and the F57W mutation in E1 is denoted by an apostrophe (E'). It should be noted that cartoons displayed throughout the figures represent only the intended arrangement of subunits, and arrangement of actual channels may vary. For MTSET and

fluorescence recordings pseudo-WT cysteine-less Q1s were used (see below). For brevity, these are called WT Q1.

All experiments were performed 24-48 hrs post transfection at room temperature. Successfully transfected cells were identified by GFP-fluorescence. For recordings in the presence of E1, currents less than 1 nA or not expressing I_{Ks} were discarded (except for E160R EQ*).

Oocyte Preparation

Mature female *Xenopus laevis* frogs (Xenopus 1, Dexter, MI, USA) were anaesthetized in a solution containing: 2 g/L tricaine methanesulfonate, 2 g/L HEPES (pH 7.4 with NaOH). Under anesthesia, the animal was euthanized in accordance with protocols approved by the University of British Columbia Animal Care Committee. The ovarian lobes were extracted, divided into smaller sections and digested for 2-4 hours in a solution containing: 3 mg/mL collagenase type 4 (Worthington Biochemical Corporation, Lakewood, NJ, USA), 82.5 mM NaCl, 2.5 mM KCl, 1 mM $MgCl_2$, 5 mM HEPES (pH 7.6 with NaOH). The oocytes were washed and stored in a media containing: 500 ml Leibovitz's L-15 medium (Thermo Fisher Scientific), 15 mM HEPES, 1 mM glutamine, 500 μM gentamycin, brought up to 1 L with distilled water (pH 7.6 with NaOH). Stage IV and V oocytes were selected and stored at 18°C.

Oocytes were injected with cRNA synthesized using the Ambion mMessage mMachine T7 transcription kit (Applied Biosystems, Foster City, California, USA). 10 ng of C214A/G219C/C331A Q1 pcDNA3.1+ (G219C Q; a gift from Dr. Jianmin Cui) cRNA was injected, while 50 ng of the tandem constructs in pGEMHE was used [C214A/G219C/C331A Q-C214A/C331A Q (G219C Q-Q), C214A/G219C/C331A Q-E160R/C214A/C331A Q* (G219C Q-E160R Q*; G219C Q-Q*) and E160R/C214A/G219C/C331A Q-C214A/C331A Q (E160R/G219C Q*-Q; G219C Q*-Q)]. The pGEMHE vector was a gift from Dr. Yoshihiro Kubo. All constructs were co-injected with 5 ng E1 pBSTA. Experiments were performed 3-4 days post injection at room temperature.

Electrophysiology Solutions

For whole cell recordings, the bath solution contained (in mM): 135 NaCl, 5 KCl, 1 $MgCl_2$, 2.8 NaAcetate, 10 HEPES (pH 7.4 with NaOH). The pipette solution contained (in mM): 130 KCl, 5 EGTA, 1 $MgCl_2$, 4 Na_2-ATP, 0.1 GTP, 10 HEPES (pH 7.2 with KOH).

For single channel recordings, the bath solution contained (in mM): 135 KCl, 1 $MgCl_2$, 1 $CaCl_2$, 10 HEPES (pH 7.4 with KOH). The pipette solution contained (in mM): 6 NaCl, 129 MES, 1 $MgCl_2$, 5 KCl, 1 $CaCl_2$, 10 HEPES (pH 7.4 with NaOH).

For two electrode voltage clamp fluorometry (VCF) experiments, the bath solution contained (in mM): 96 NaCl, 3 KCl, 1 $MgCl_2$, 2 $CaCl_2$, 0.1 $LaCl_3$, 5 HEPES (pH 7.4 with NaOH). The pipette solution contained 3 M KCl.

Patch Clamp Electrophysiology

Whole cell and single channel currents were acquired using an Axopatch 200B amplifier, Digidata 1440A and pClamp 10 software (Molecular Devices, San Jose, CA, USA). For whole cell recordings, a linear multistage electrode puller (Sutter Instrument, Novato, CA, USA) was used to pull electrode pipettes from thin-walled borosilicate glass (World Precision Instruments, Sarasota, FL, USA) (1, 2). Pipettes were fire-polished prior to use. Electrode resistances for whole cell recordings were between 1-2 MΩ, with series resistances <4 MΩ. Series resistance compensation of ~80% was applied to all whole cell recordings, with a calculated voltage error of ~1 mV/nA current. Whole cell currents were sampled at 10 kHz and filtered at 2-5 kHz (1, 2).

Single channel electrodes were pulled from thick-walled borosilicate glass (Sutter Instrument) using the linear multistage electrode puller (Sutter Instrument). Electrodes were coated with Sylgard (Dow Corning, Midland, MI, USA). After fire polishing, single channel electrode resistances were between 40 and 60 MΩ (1, 3-5).

Two electrode voltage clamp experiments were performed using an Oocyte Clamp OC-725C (Warner Instruments, Hamden, CT, USA) and digitized using a Digidata 1440A (Molecular Devices) using the pClamp 10 software (Molecular Devices).

TEA^+ Experiments

WT EQQ + E1, V319Y EQQ + E1 and E160R/V319Y EQ*Q (V319Y EQ*Q) + E1 were expressed in tsA201 cells. Tetraethylammonium chloride (TEA^+) was made up to the desired stock concentration in whole cell patch clamp bath solution. After currents reached a stable baseline of 5 sweeps, 0.5, 2, 5, 20, and 50 mM TEA^+ was added to the bath. After the effect of TEA^+ had stabilized, the TEA^+ was washed off with the external bath solution. No correction was made for solution osmolality upon addition of TEA^+.

MTSET Experiments

C214A/G229C/C331A Q-E160R/C214A/C331A Q* (G229C Q-E160R Q*; G229C Q-Q*) + E1 or E160R/C214A/G229C/C331A Q*-C214A/C331A Q (E160R/G229C Q*-Q; G229C Q*-Q) + E1 were expressed in tsA201 cells. MTSET was made up to the desired stock concentration in whole cell external bath solution and aliquots were flash frozen in liquid nitrogen and stored at -80°C before use. While waiting for the current to reach a stable baseline, MTSET aliquots were removed from the freezer and kept on ice. 2 mM MTSET was added to the bath after the current maintained a stable baseline for five sweeps.

VCF Experiments

Oocytes were labelled with 10 μM Alexa Fluor 488 C_5-maleimide in a depolarizing high potassium solution containing (in mM): 98 KCl, 1.8 $CaCl_2$, 5 HEPES (pH 7.6 with KOH) for 30 minutes on ice. The oocytes were washed with the bath solution and left on ice prior to recording. Fluorescence and ionic recordings were obtained simultaneously as previously described (6) with an Omega XF100-2 filter set (Omega Optical Inc, Brattleboro, VT, USA). Fluorescence recordings from the same oocyte were averaged to reduce signal noise errors. To correct for photobleaching, a fluorescence signal was recorded in the absence of a voltage step, and was subtracted from the signal.

Data analysis

Conductance-Voltage (G-V) plots were obtained from tail current amplitudes. A Boltzmann sigmoidal equation was used to fit G-Vs (Prism 7, GraphPad Software, La

Jolla, CA) to obtain the $V_{1/2}$ and slope factor. All the $V_{1/2}$s of activations and k-factors for the Q1 constructs in the presence and absence of E1 are shown in SI Appendix, Table S1. Fluorescence-Voltage (F-V) plots were fit with a double Boltzmann equation (Prism 7, GraphPad Software). Current activation waveforms were fit with a single exponential equation in Prism 7, with the fit starting at 0.5 s. Deactivation curves were fit with a single exponential curve in Prism 7 for all 4 s of the deactivating pulse to extract time constants.

Single-channel current records were low-pass filtered at 2 kHz at acquisition using a −3dB, four-pole Bessel filter, sampled at 10 kHz, and digitally filtered at 200 Hz before analysis.

All results are reported as mean ± SE, unless otherwise stated. Statistical comparison was performed using either a one-way ANOVA with Tukey's post hoc test or a two-tailed Student's t-test. p-values less than 0.05 were considered to be statistically significant.

Modeling

Markov modeling in Figure 9 was performed using the IonChannelLab software (7) incorporating Q-matrix solutions to the differential equations defining the kinetic behavior of rate transitions (8). The software is freely available on the internet and may be found at http://www.jadesantiago.com/Electrophysiology/IonChannelLab/

The balanced Zaydman 2014 model (9) for the four VS channel was constructed as published using the same notation for rates and constants. Charge valence for the VS transitions was not altered. Voltage-dependent rates were scaled down to better match control mammalian cell activation and deactivation data. This was a factor of 10x for the k_{IR} and k_{RI} transitions, 7.4x for k_{IA} and 13.7x for k_{AI} (values in SI Appendix, Table S2); the voltage-dependences of the rates are shown graphically in the SI Appendix, Figure S13.

The equations used to calculate k_{CO} and k_{OC} values were: Opening rate = $k_{CO}/(\Theta_{RC}^{n(R)} * \Theta_{IC}^{n(I)} * \Theta_{AC}^{n(A)})$. Closing rate = $k_{OC}/(\Theta_{RO}^{n(R)} * \Theta_{IO}^{n(I)} * \Theta_{AO}^{n(A)})$, where the closed to open transitions depend upon the intrinsic rate of the pore (k_{CO}) divided by the product of the closed state interactions of the VSs. The open to closed transitions depend upon the k_{OC} divided by the product of the open state interactions of the VSs. The exponent n(R, I,

or A) indicates the number of VSs in states R, I, or A. The Θ values were unchanged from Zaydman et al. (2014) (9).

To simulate the number of E160R non-activatable subunits in each construct, the number of VSs was reduced in the model from four in control to as low as one to simulate E160R EQ*QQ*Q* + E1. This assumed independence of movement of individual subunits. These models are depicted in the diagrams in SI Appendix, Figure S12.

The open state conductance was varied depending on the number of activated VS, using the relative values obtained from single channel data in this paper and published previously (4). The conductances for the different numbered open states (O^x) in SI Appendix, Figure S12 are stated in SI Appendix, Table S2.

Simulations were generally run as a 4 s depolarization and 2 s repolarization, and so data tended to be isochronal and not steady state, in order to better match experimental protocols. Data from simulations were exported to Excel (Microsoft Office, Redmond, WA, USA) for analysis and fitting using the SOLVER module. All values for rate constants and other constants may be found in SI Appendix, Table S2, and the calculations for each C-C and O-O transition may be found in SI Appendix, Tables S3 and S4.

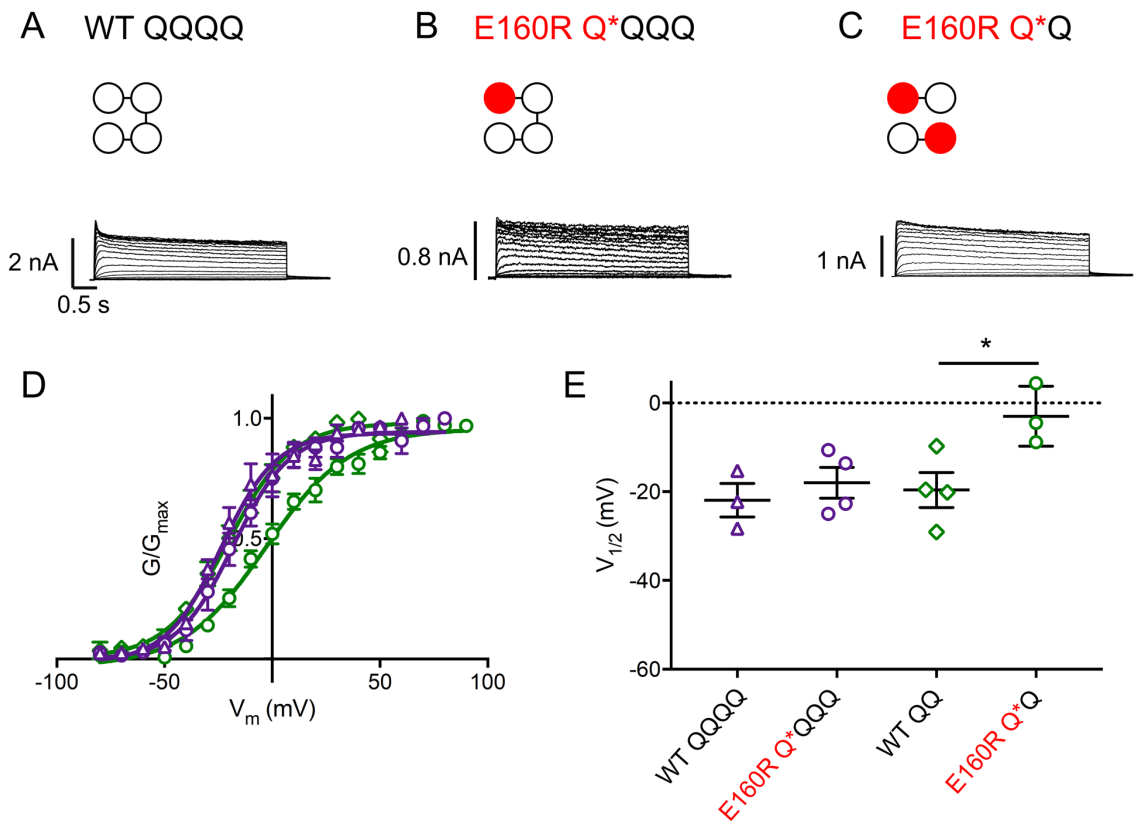

Figure S1. When expressed without E1, channel complexes with one or two E160R mutations produce functional currents. Currents were obtained using the same isochronal activation protocol as shown in Figure 2B. Representative currents are shown for WT QQQQ (A), E160R Q*QQQ (B), and E160R Q*Q (C). Cartoons describe the mutations in the constructs: WT Q1 (unfilled circles) and E160R Q1 (red circles). Black lines indicate tethers between subunits. (D) G-V plots of WT QQQQ (open purple triangles), E160R Q*QQQ (open purple circles), WT QQ (open green diamonds) and E160R Q*Q (open green circles). (E) Summary of the $V_{1/2}$s of activation for each construct (n = 3-4; * = $p<0.05$, SI Appendix, Table S1). Error bars denote mean ± SE.

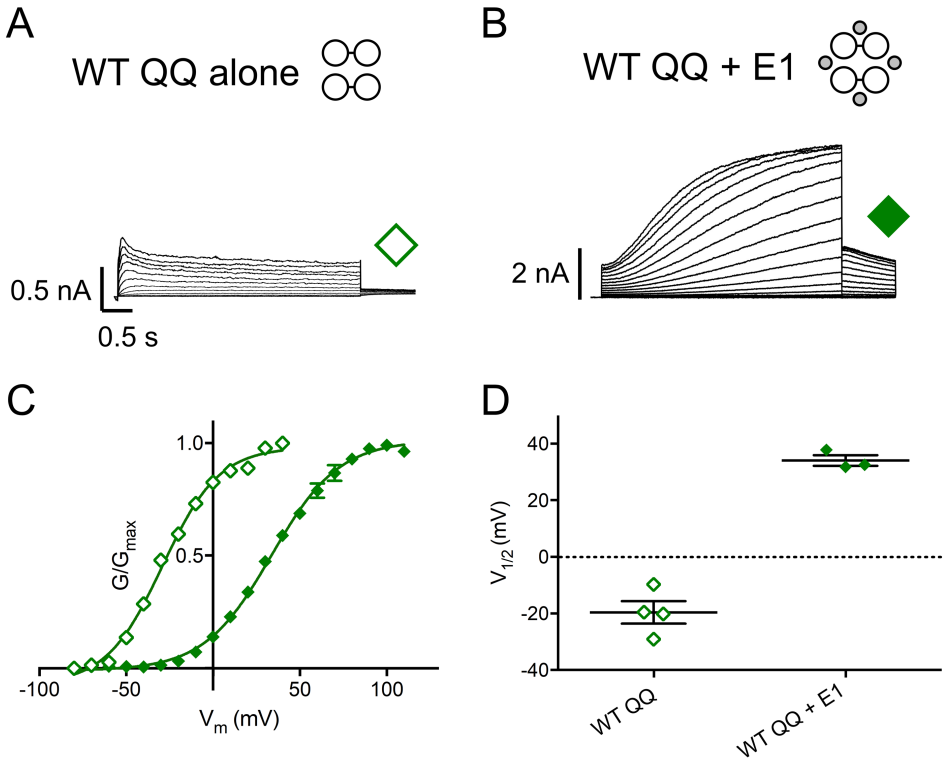

Figure S2. WT QQ alone and co-expressed with E1. Currents were obtained using the same isochronal activation protocol described in Figure 2B. A representative set of currents is shown for WT QQ alone (A) and WT QQ + E1 (B). Cartoons describe the constructs: E1 (small grey circles) and WT Q1 (unfilled circles). Black lines indicate tethers between subunits. (C) G-V plots of WT QQ alone (open green diamonds) and WT QQ + E1 (closed green diamonds). (D) Summary of the $V_{1/2}$s of activation of each construct (n = 3-4; SI Appendix, Table S1). Error bars denote mean ± SE.

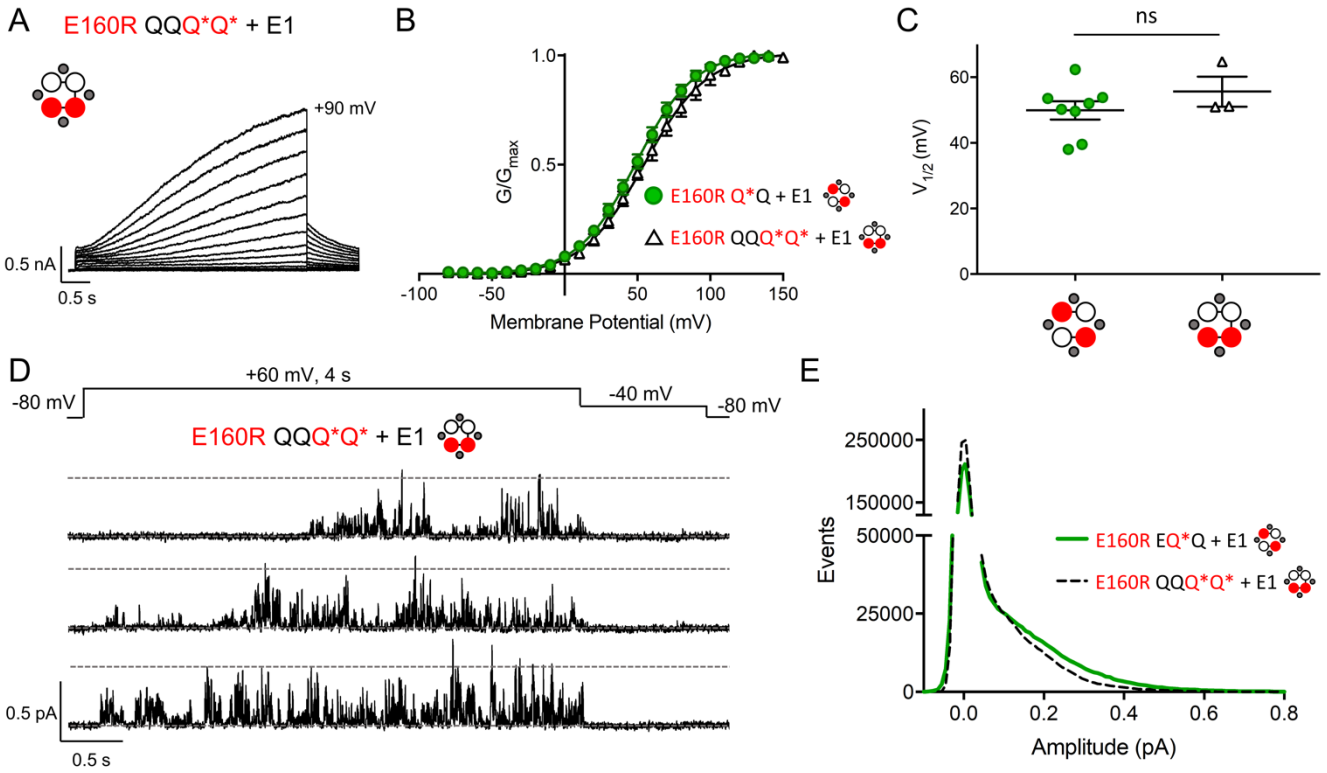

Figure S3. Activation kinetics of E160R QQQ*Q* + E1 are similar to E160R Q*Q + E1. Currents were obtained using the same isochronal activation protocol described in Figure 2B. (A) A representative set of currents is shown for E160R QQQ*Q* + E1. Cartoons describe the mutations in the constructs: E1 (small grey circles), WT Q1 (unfilled circles) and E160R Q1 (red circles). Black lines indicate tethers between subunits. (B) G-V plots of E160R Q*Q + E1 (green circles) and E160R QQQ*Q* + E1 (open black triangles). (C) Summary of the $V_{1/2}$ of activation for each construct (n = 3-8; p-value = 0.31; SI Appendix, Table S1). (D) Representative single channel sweeps of E160R QQQ*Q* + E1. Cells were pulsed to +60 mV for 4 s, followed by a tail current at -40 mV. (E) All points-histogram of 39 active sweeps of E160R EQ*Q + E1 (green line; n = 3) and 39 active sweeps of E160R QQQ*Q* + E1 (dashed black line; n = 1). Error bars denote mean ± SE.

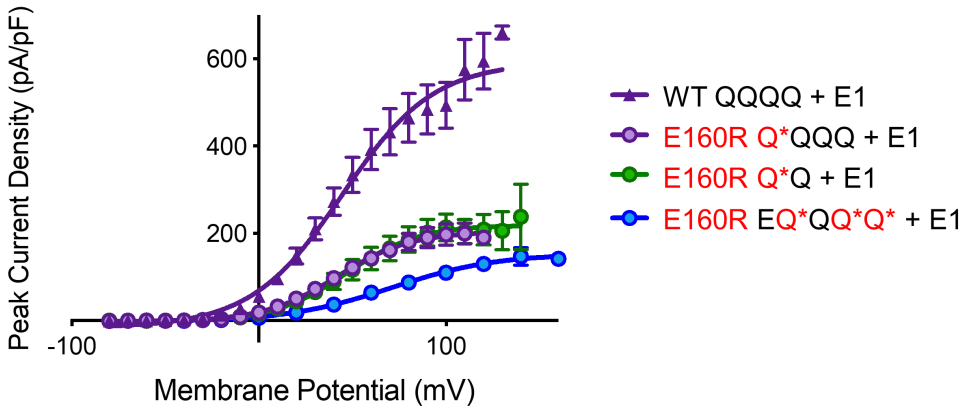

Figure S4. E160R reduces peak current density. Peak current density is plotted versus membrane potential for WT QQQQ + E1 (purple triangles, n = 7), E160R Q*QQQ + E1 (purple circles, n = 5), E160R Q*Q + E1 (green circles, n = 8), E160R EQ*QQ*Q* + E1 (blue circles, n = 3). Error bars denote mean ± SE.

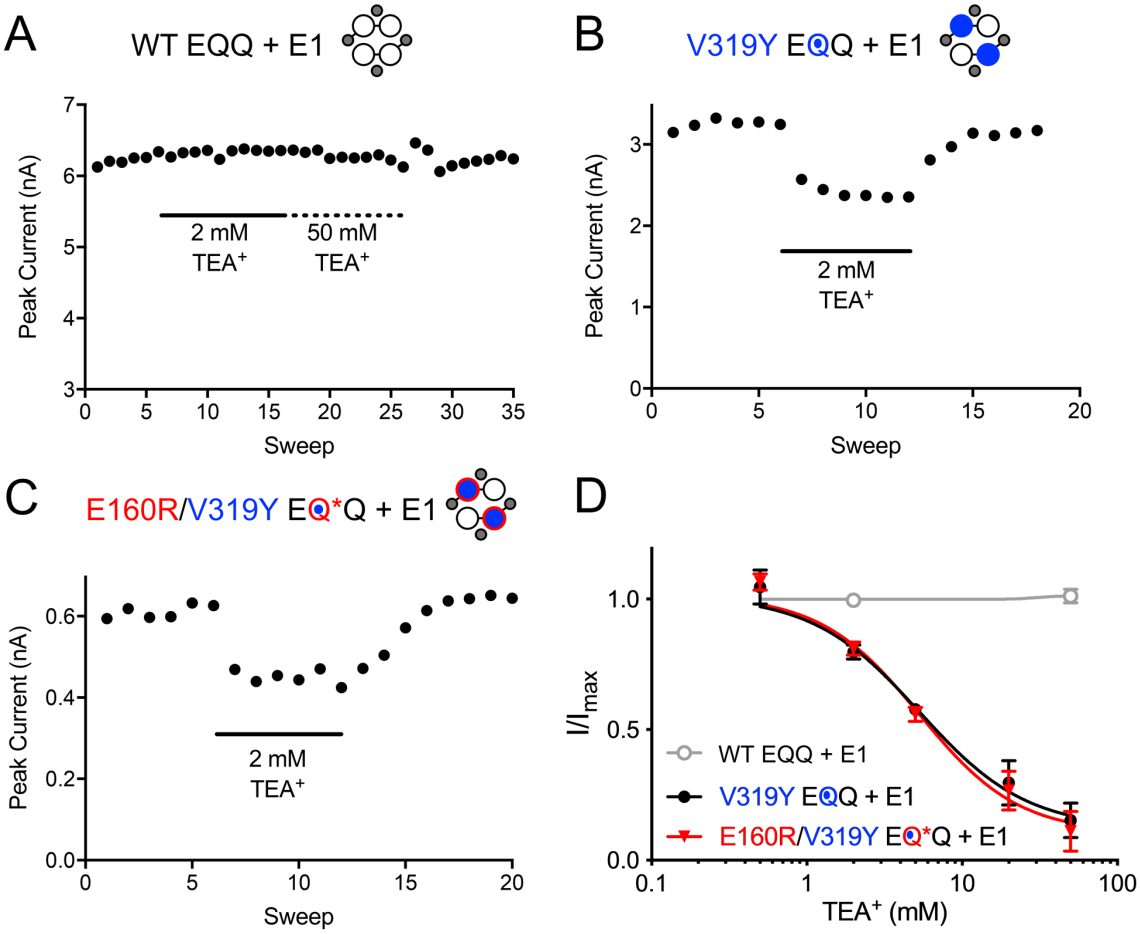

Figure S5. TEA$^+$ sensitivity reveals mutated E160R subunits are not excluded from channel assembly. Currents were obtained by pulsing to +60 mV or +80 mV for 4 s, followed by -40 mV for 0.9 s. The sweep to sweep interval was 15 s. Representative current diary plots for WT EQQ + E1 (A), V319Y EQQ + E1 (B) and E160R/V319Y EQ*Q + E1 (C) showing peak current at +60 or +80 mV vs sweep number. The solid black line indicates addition of 2 mM TEA$^+$ and the dashed line indicates addition of 50 mM TEA$^+$. Cartoons describe the mutations in the constructs: E1 (small grey circles), WT Q1 (unfilled circles), V319Y Q1 (blue circles) and E160R/V319Y Q1 (blue circles with red border). Black lines indicate tethers between subunits. (D) TEA$^+$ dose-response curves are shown for WT EQQ + E1 (grey circles, 2 mM (n =1) and 50 mM (n = 4)), V319Y EQQ + E1 (black circles, 0.5 mM (n = 3), 2 mM (n = 6), 5 mM (n = 3), 20 mM (n = 3), 50 mM (n = 4); IC_{50} = 5.3 mM; Hill Coefficient = 1.3) and E160R/V319Y EQ*Q + E1 (red triangles, 0.5 mM (n = 3), 2 mM (n = 4), 5 mM (n = 3), 20 mM (n = 4) and 50 mM (n =3); IC_{50} = 5.3 mM; Hill Coefficient = 1.4). Error bars denote mean ± SE.

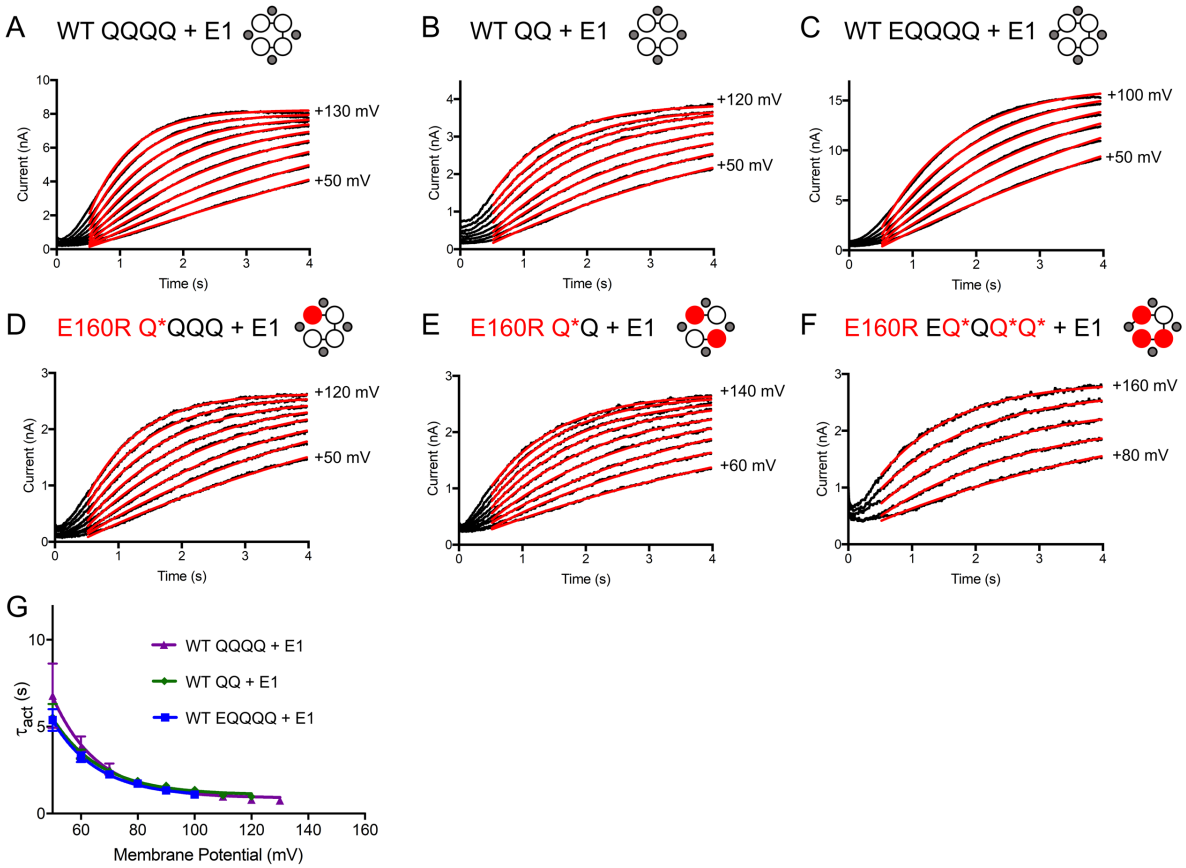

Figure S6. Representative single exponential fits to activating current waveforms. Representative sets of currents during activation to a range of potentials, fit with a single exponential function (red line) starting at 0.5 s for WT QQQQ + E1 (A), WT QQ + E1 (B), WT EQQQQ + E1 (C), E160R Q*QQQ + E1 (D), E160R Q*Q + E1 (E) and E160R EQ*QQ*Q* + E1 (F). Membrane current at each membrane potential was fit with a single exponential equation to produce a time constant of activation (τ_{act}) for each construct at each voltage. Cartoons describe the mutations in the constructs: E1 (small grey circles), WT Q1 (unfilled circles) and E160R Q1 (red circles). Black lines indicate tethers between subunits. (G) The time constants of activation (τ_{act}) at various membrane potentials are plotted for WT QQQQ + E1 (purple triangles), WT QQ + E1 (green diamonds) and WT EQQQQ + E1 (blue squares) (n = 3-7). No significant differences were found between values for different WT constructs. Error bars denote mean ± SE.

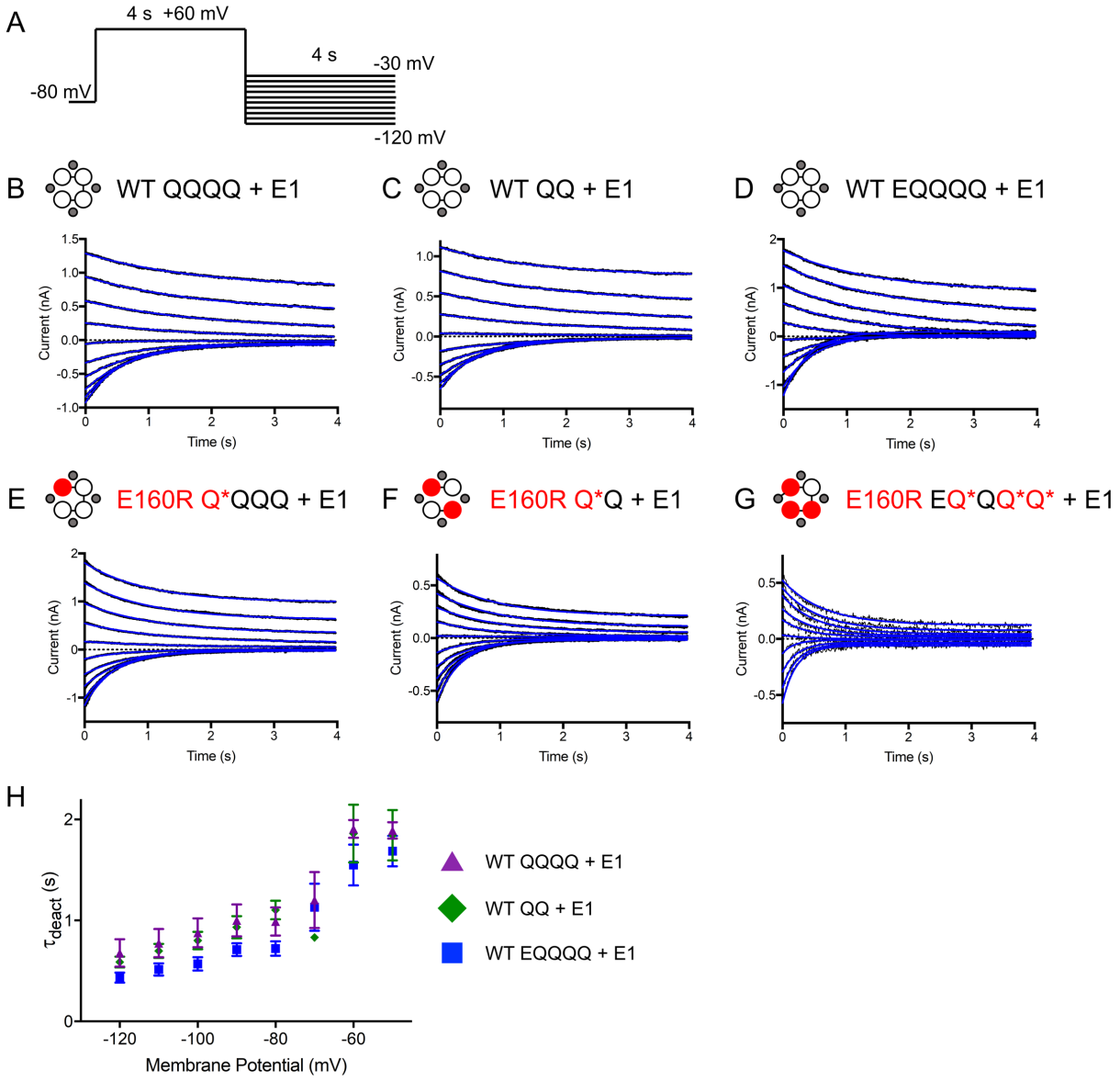

Figure S7. Representative single exponential fits to tail currents. (A) Deactivation protocol used to obtain tail currents. Cells were held at -80 mV, and pulsed to +60 mV for 4 s followed by a 4 s pulse to a range of potentials from -30 to -120 mV in 10 mV steps, to record tail currents. Representative set of tail currents with a single exponential fit (blue line) for WT QQQQ + E1 (B), WT QQ + E1 (C), WT EQQQQ + E1 (D), E160R Q*QQQ + E1 (E), E160R Q*Q + E1 (F) and E160R EQ*QQ*Q* + E1 (G). Cartoons describe the mutations in the constructs: E1 (small grey circles), WT Q1 (unfilled circles) and E160R Q1 (red circles). Black lines indicate tethers between subunits. (H) Time constants of deactivation (τ_{deact}) at various membrane potentials were plotted for WT QQQQ + E1 (purple triangles), WT QQ + E1 (green diamonds) and WT EQQQQ + E1 (blue squares) (n = 4-7). No significant differences were found between values for different WT constructs. Error bars denote mean ± SE.

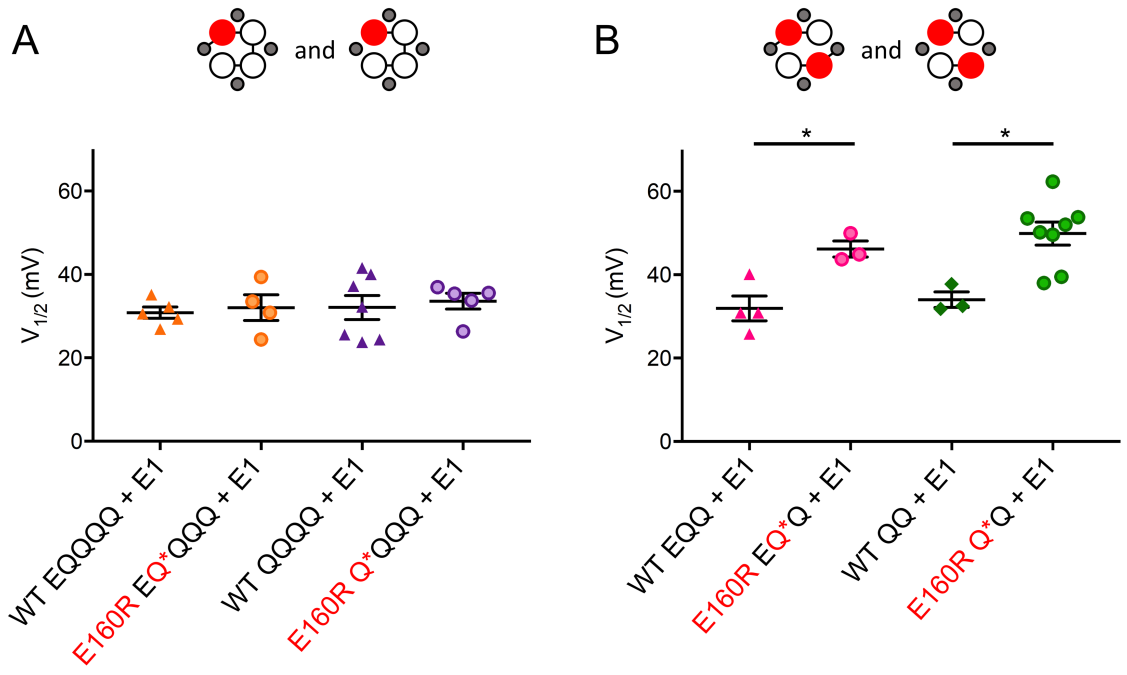

Figure S8. Channel complexes with a tethered E1 produce a similar result to the untethered constructs. (A) Summary of the $V_{1/2}$ of activation for channels containing one E160R mutant compared to WT: WT EQQQQ + E1 (orange triangles), E160R EQ*QQQ + E1 (orange circles), WT QQQQ + E1 (purple triangles) and E160R Q*QQQ + E1 (purple circles) (n = 4-7; SI Appendix, Table S1). (B) Summary of the $V_{1/2}$ of activation for channels containing two E160R mutants compared to WT: WT EQQ + E1 (pink triangles), E160R EQ*Q + E1 (pink circles), WT QQ + E1 (green diamonds) and E160R Q*Q + E1 (green circles) (n = 3-8; * = $p<0.05$; SI Appendix, Table S1). Cartoons describe the mutations in the constructs: E1 (small grey circles), WT Q1 (unfilled circles) and E160R Q1 (red circles). Black lines indicate tethers between subunits. Error bars denote mean ± SE.

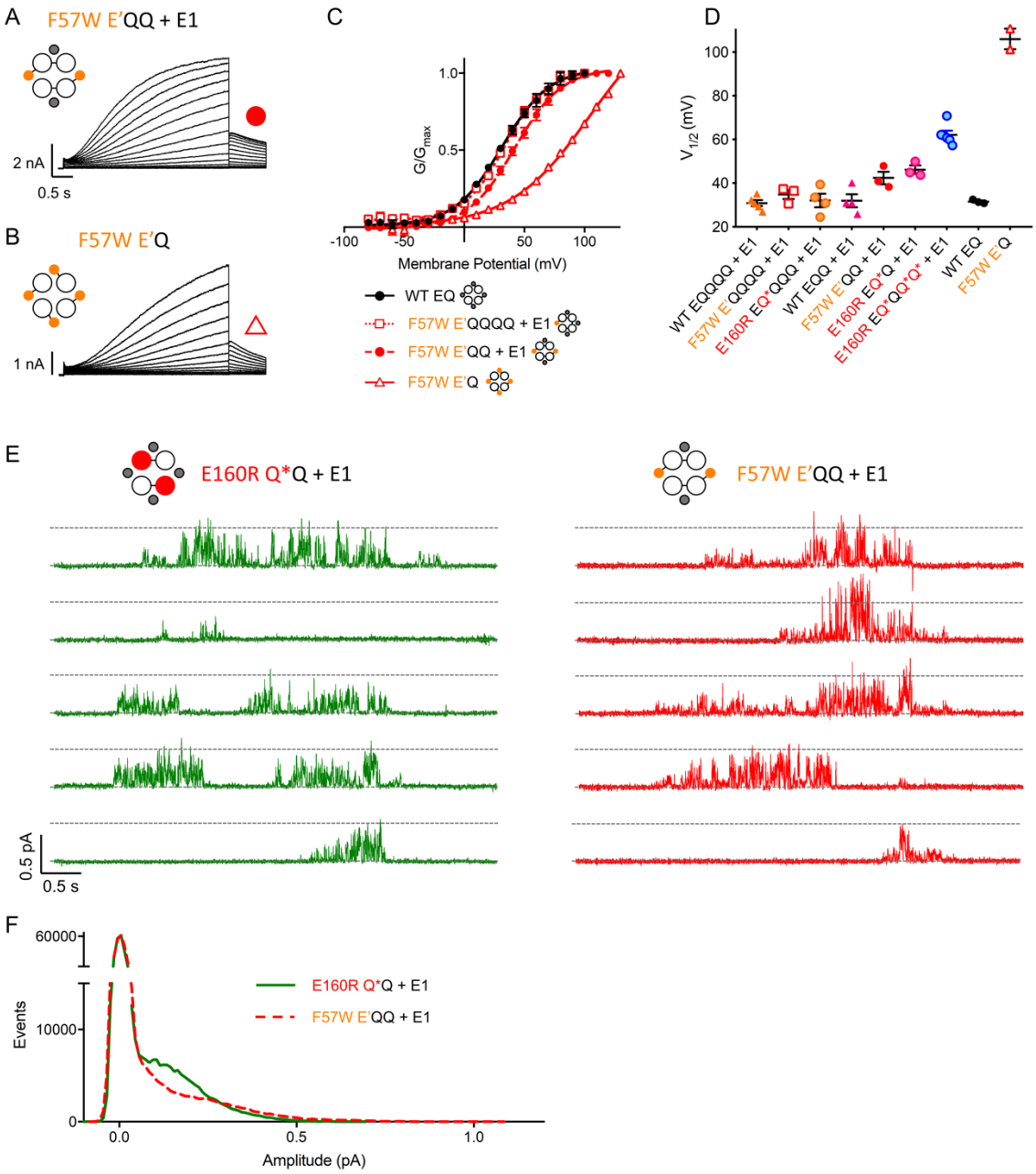

Figure S9. Effect of one, two or four KCNE1 F57W mutations on the I_{Ks} channel. Currents were obtained using the same isochronal activation protocol described in Figure 2B. Representative currents are shown for F57W E'QQ + E1 (A) and F57W E'Q (B). Cartoons describe the mutations in the constructs: WT E1 (small grey circles), F57W E1 (small orange circles), E160R Q1 (red circles) and WT Q1 (unfilled circles). Black lines indicate tethers between subunits. (C) G-V plots of WT EQ (black circles), F57W E'QQQQ + E1 (open red squares), F57W E'QQ + E1 (red circles) and F57W E'Q (open red triangles). (D) Summary of the $V_{1/2}$s of activation of WT, F57W and E160R constructs (n = 2-6; SI Appendix, Table S1). (E) Representative single channel recordings of E160R Q*Q + E1 (left) and F57W E'QQ + E1 (right). Membrane patches containing a single

mutant I_{Ks} channel were stepped from -80 to +60 mV for 4 s and then to -40 mV for 0.8 s as shown in Figure 5A. (F) All-points amplitude histogram of 10 active E160R Q*Q + E1 sweeps (green line) and 10 active F57W E'QQ + E1 sweeps (dashed red line). Error bars denote mean ± SE.

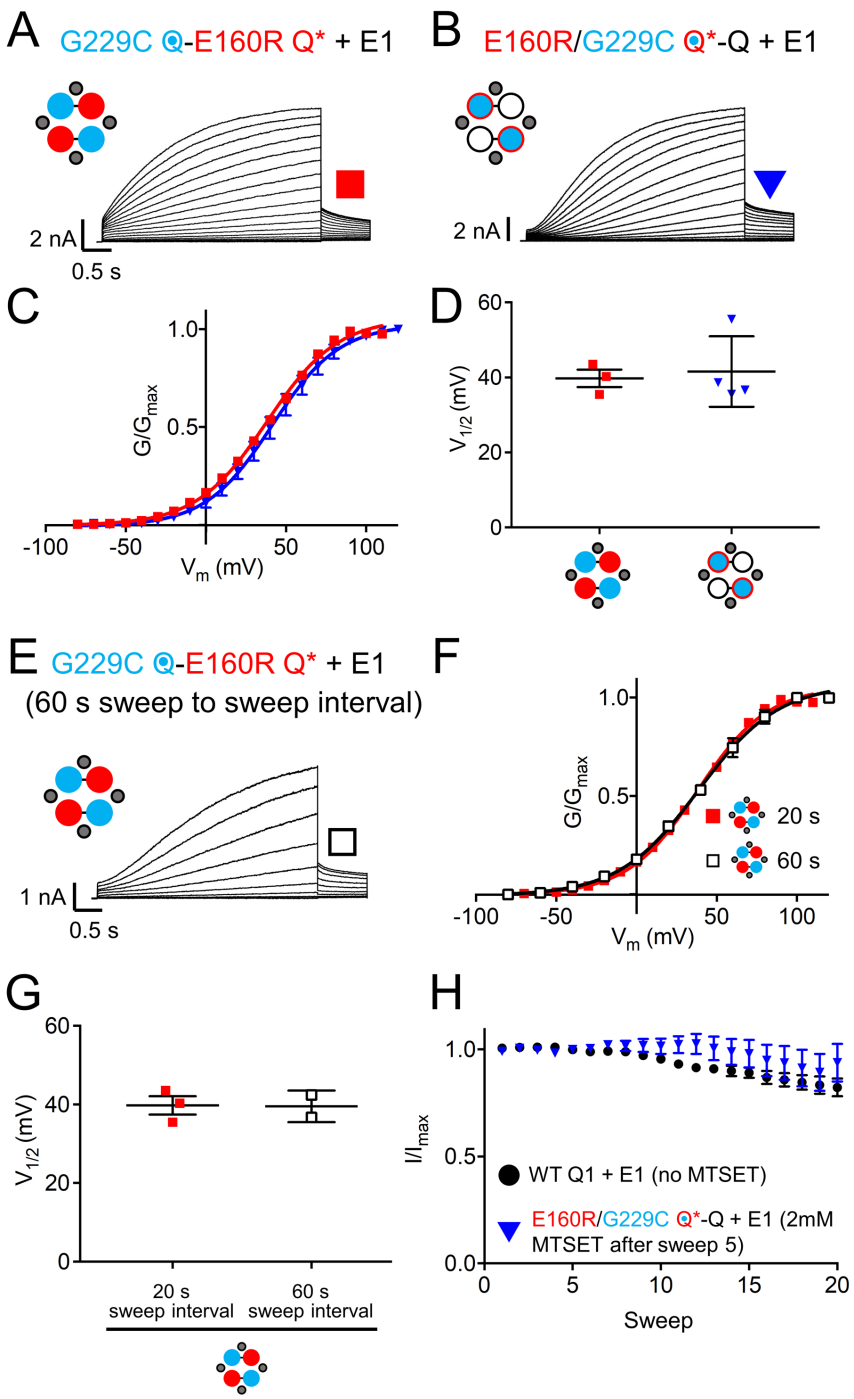

Figure S10. Additional MTSET information. Currents were obtained using the same isochronal activation protocol as shown in Figure 2B. The sweep to sweep interval was 20 s. Representative currents are shown for G229C Q-E160R Q* + E1 (A) and E160R/G229C Q*-Q + E1 (B). Cartoons describe the mutations in the constructs: E1 (small grey circles), WT Q1 (unfilled circles), E160R Q1 (red circles), G229C Q1 (blue circles), E160R/G229C Q1 (blue circles with red border). Black lines indicate tethers between subunits. (C) G-V plots of G229C Q-E160R Q* + E1 (red squares) and E160R/G229C Q*-Q + E1 (blue triangles). (D) Summary of the $V_{1/2}$ of activation for each

construct (n = 3-4; See SI Appendix, Table S1). Holding G229C Q-E160R Q* + E1 channels longer between sweeps results in more sigmoidal currents. Currents were obtained using a similar isochronal activation protocol as shown in Figure 2B, however voltage steps were 20 mV and the sweep to sweep interval was 60 s. (E) A representative set of currents is shown for G229C Q-E160R Q* + E. (F) G-V plots of G229C Q-E160R Q* + E1 with sweep to sweep intervals of 20 s (red squares) and 60 s (open black squares). (G) Summary of the $V_{1/2}$ of activation for each construct (n = 2-3). (H) Normalized peak current over 20 sweeps for WT Q1 + E1 in the absence of MTSET (black circles, n = 4) and E160R/G229C Q*-Q + E1 in the presence of 2 mM MTSET after sweep 5 (blue triangles, n = 6) is shown. Error bars denote mean ± SE.

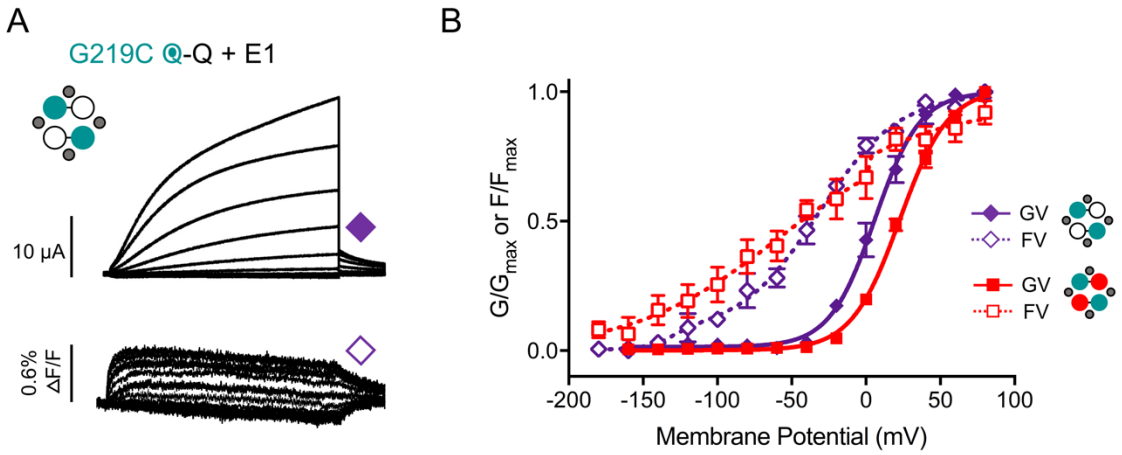

Figure S11. VCF recordings of G219C Q-Q + E1 channels. VCF recordings were obtained using the same protocol as described in Figure 8A. Representative current (upper) and fluorescence (lower) recordings are shown for G219C Q-Q + E1 (A). Cartoons describe the mutations in the constructs: E1 (small grey circles), WT Q1 (unfilled circles), G219C Q1 (teal circles) and E160R Q1 (red circles). Black lines indicate tethers between subunits. (B) G-V and F-V plots are shown for G219C Q-Q + E1 (G-V: closed purple diamonds and F-V: open purple diamonds) and G219C Q-E160R Q* + E1 (G-V: closed red squares and F-V: open red squares) (n = 2-7). Error bars denote mean ± SE.

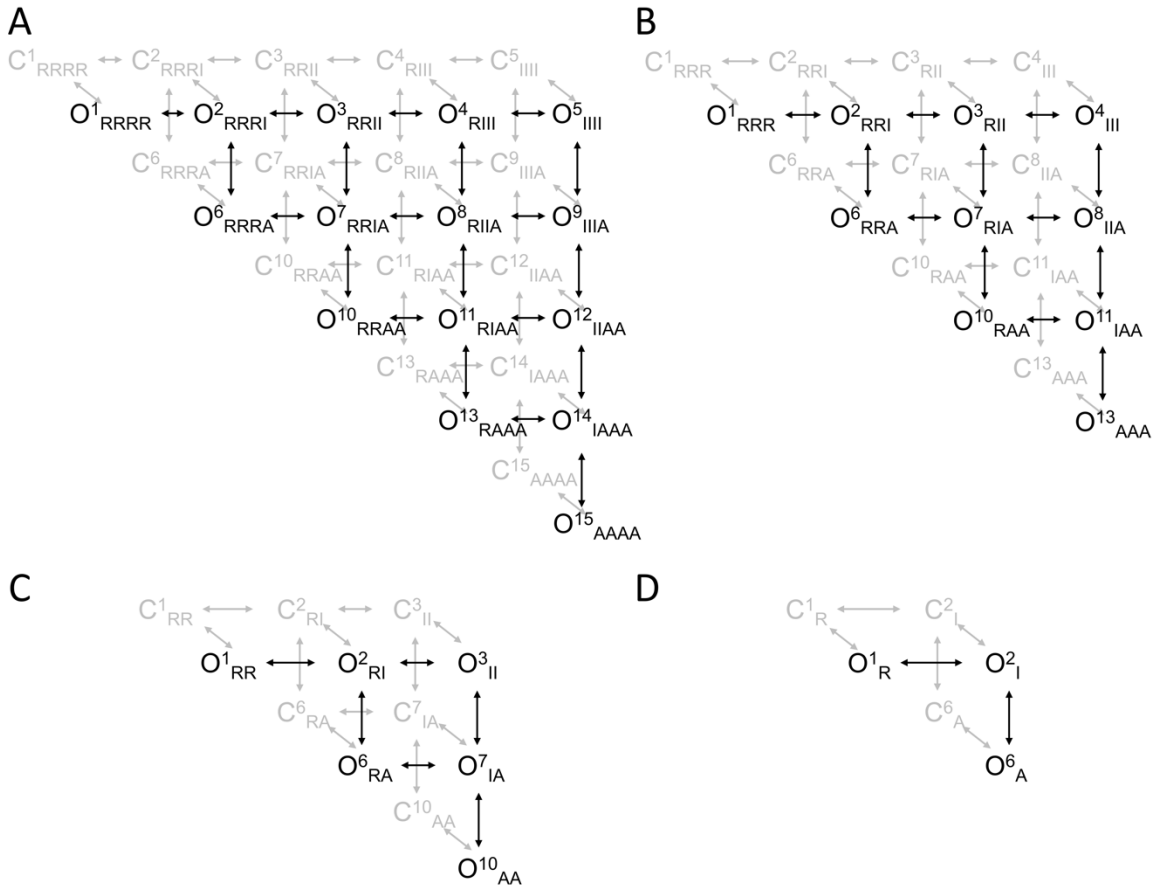

Figure S12. Schematic diagrams of allosteric models. Schematics of allosteric models with four (A), three (B), two (C) or one (D) functional VSs are displayed. Resting, intermediate and activated states of the VSs are represented by 'R', 'I' and 'A' respectively. Closed and open states are represented by 'C' and 'O' respectively. Numbering of open states (O^x) is for reference to conductance values in SI Appendix, Table S2. Transition rates of the VS and pore as well as VS-pore interactions are as described in SI Appendix, Tables S2-S4.

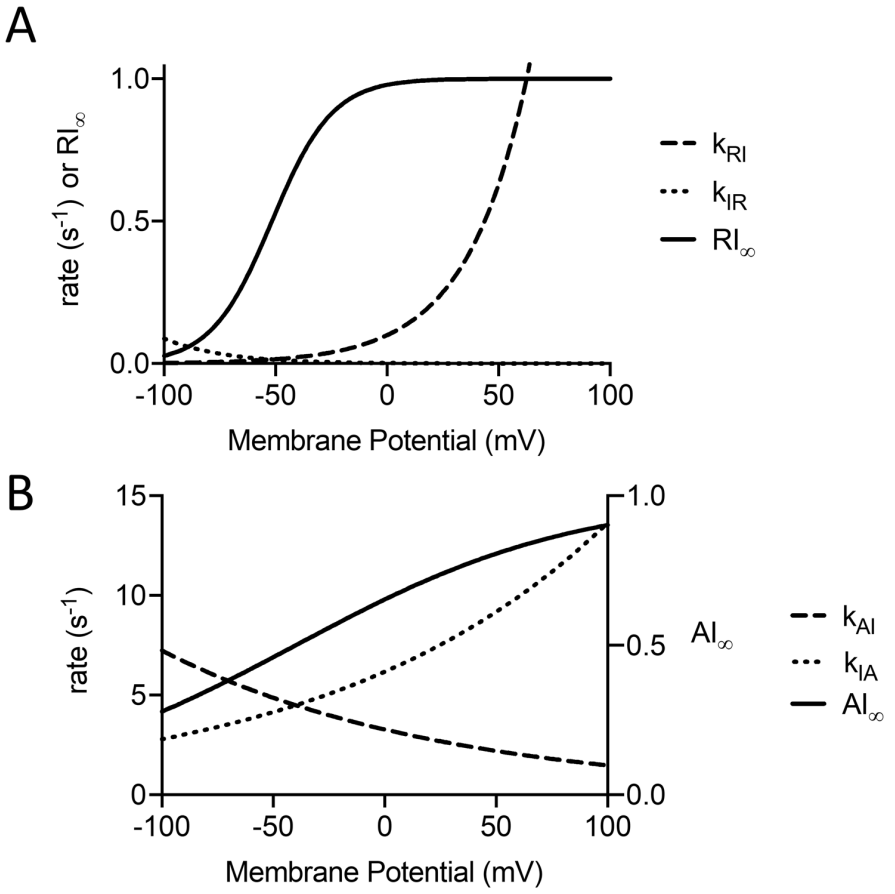

Figure S13. Voltage-dependent model rates. Rate constants for VS movements from resting to intermediate states (A, dashed line) and intermediate to resting states (A, dotted line) are plotted versus voltage. The equilibrium for the transition, $k_{RI}/(k_{RI}+k_{IR})$, is shown by the solid line, RI_∞. Rate constants for VS movements from activated to intermediate (B, dashed line) and intermediate to activated (B, dotted line) are plotted versus voltage dependence. The equilibrium for the transition, $k_{IA}/(k_{IA}+k_{AI})$, is represented by the solid line, AI_∞.

Table S1. $V_{1/2}$ of activation for Q1 constructs in the presence and absence of E1.

Construct	$V_{1/2}$ (mV) mean ± SEM	p-values compared with $V_{1/2}$ of WT EQ	k-factor mean ± SEM	n (cells)
WT QQQQ	-21.9 ± 3.8	-	13.6 ± 3.9	3
WT QQQQ + E1	32.1 ± 2.9	0.9998	19.9 ± 0.7	7
WT EQQQQ + E1[†]	30.9 ± 1.4	0.9998	18.0 ± 1.6	5
WT QQ	-19.6 ± 3.9	-	14.5 ± 1.4	4
WT QQ + E1	34.1 ± 1.9	0.9992	19.7 ± 1.7	3
WT EQQ + E1[†]	31.9 ± 3.0	0.9999	20.2 ± 1.4	4
WT Q1 + E1[†]	26.1 ± 2.2	0.7397	23.1 ± 1.4	11
WT EQ	31.5 ± 0.5	-	20.0 ± 1.2	3
E160R Q*QQQ	-18.0 ± 3.5	-	13.1 ± 0.2	4
E160R Q*QQQ + E1	33.6 ± 1.9	0.9993	17.6 ± 0.9	5
E160R EQ*QQQ + E1	32.0 ± 3.1	0.9999	17.9 ± 0.8	4
E160R Q*Q	-3.0 ± 3.9	-	18.6 ± 2.2	3
E160R Q*Q + E1	49.9 ± 2.8	0.0005	20.0 ± 0.9	8
E160R EQ*Q + E1	46.2 ± 1.9	0.0410	21.4 ± 1.4	3
E160R QQQ*Q* + E1	55.6 ± 4.6	0.0002	21.6 ± 2.7	3
E160R EQ*QQ*Q* + E1	62.1 ± 1.9	<0.0001	22.7 ± 0.7	6
F57W E'QQQQ + E1	34.8 ± 2.1	0.9958	17.3 ± 0.8	3
F57W E'QQ + E1	42.3 ± 2.9	0.2273	20.0 ± 0.5	3
F57W E'Q	106.0 ± 4.7	<0.0001	33.8 ± 2.2	2
G229C Q-E160R Q* + E1	39.8 ± 2.3	-	23.0 ± 1.3	3
E160R/G229C Q*-Q + E1	41.6 ± 4.7	-	20.5 ± 0.8	4
G219C Q + E1	20.9 ± 6.4	-	21.3 ± 0.8	5
G219C Q-Q + E1	6.1 ± 4.6	-	15.2 ± 1.4	2
G219C Q-E160R Q* + E1	23.5 ± 1.8	-	16.5 ± 1.1	6
E160R/G219C Q*-Q + E1	19.4 ± 6.5	-	17.3 ± 2.5	3

[†] Data from ref. 1

Table S2. Rates and constants used in the model. Modified from ref. 9, which is licensed under CC BY 4.0.

	Description	Value	Units
$k_{RI}0$	Intrinsic R→I rate at 0 mV	0.1	s^{-1}
z_{RI}	Intrinsic R → I valence	0.93	C
$k_{IR}0$	Intrinsic I → R rate at 0 mV	$2.22e^{-3}$	s^{-1}
z_{IR}	Intrinsic I → R valence	-0.93	C
$k_{IA}0$	Intrinsic I → A rate at 0 mV	6.1777	s^{-1}
z_{IA}	Intrinsic I → A valence	0.2	C
$k_{AI}0$	Intrinsic A → I rate at 0 mV	3.2778	s^{-1}
z_{AI}	Intrinsic A → I valence	-0.2	C
k_{co}	Intrinsic C → O rate	100	s^{-1}
k_{oc}	Intrinsic O → C rate	500	s^{-1}
θ_{RC}	VSD-pore interactions in RC	1	
θ_{RO}	VSD-pore interactions in RO	1	
θ_{IC}	VSD-pore interactions in IC	10	
θ_{IO}	VSD-pore interactions in IO	1.68	
θ_{AC}	VSD-pore interactions in AC	0.9	
θ_{AO}	VSD-pore interactions in AO	16.8	
O^1-O^5	Conductance of resting open state	0.07	pS
O^6-O^9	Conductance of single active VS open state	1.38	pS
O^{10}-O^{12}	Conductance of two activated VS open state	2.1	pS
O^{13}-O^{14}	Conductance of three activated VS open state	3.2	pS
O^{15}	Conductance of four activated VS open state	4.8	pS

Table S3. Transition rates between model closed states.

# of activatable VSs	4		3		2		1	
	Forward	Reverse	Forward	Reverse	Forward	Reverse	Forward	Reverse
$C^1 \leftrightarrow C^2$	$4k_{RI}/\theta_{RC}$	k_{IR}/θ_{IC}	$3k_{RI}/\theta_{RC}$	k_{IR}/θ_{IC}	$2k_{RI}/\theta_{RC}$	k_{IR}/θ_{IC}	k_{RI}/θ_{RC}	k_{IR}/θ_{IC}
$C^2 \leftrightarrow C^3$	$3k_{RI}/\theta_{RC}$	$2k_{IR}/\theta_{IC}$	$2k_{RI}/\theta_{RC}$	$2k_{IR}/\theta_{IC}$	k_{RI}/θ_{RC}	$2k_{IR}/\theta_{IC}$	-	-
$C^3 \leftrightarrow C^4$	$2k_{RI}/\theta_{RC}$	$3k_{IR}/\theta_{IC}$	k_{RI}/θ_{RC}	$3k_{IR}/\theta_{IC}$	-	-	-	-
$C^4 \leftrightarrow C^5$	k_{RI}/θ_{RC}	$4k_{IR}/\theta_{IC}$	-	-	-	-	-	-
$C^2 \leftrightarrow C^6$	k_{IA}/θ_{IC}	k_{AI}/θ_{AC}	k_{IA}/θ_{IC}	k_{AI}/θ_{AC}	k_{IA}/θ_{IC}	k_{AI}/θ_{AC}	k_{IA}/θ_{IC}	k_{AI}/θ_{AC}
$C^3 \leftrightarrow C^7$	$2k_{IA}/\theta_{IC}$	k_{AI}/θ_{AC}	$2k_{IA}/\theta_{IC}$	k_{AI}/θ_{AC}	$2k_{IA}/\theta_{IC}$	k_{AI}/θ_{AC}	-	-
$C^4 \leftrightarrow C^8$	$3k_{IA}/\theta_{IC}$	k_{AI}/θ_{AC}	$3k_{IA}/\theta_{IC}$	k_{AI}/θ_{AC}	-	-	-	-
$C^5 \leftrightarrow C^9$	$4k_{IA}/\theta_{IC}$	k_{AI}/θ_{AC}	-	-	-	-	-	-
$C^6 \leftrightarrow C^7$	$3k_{RI}/\theta_{RC}$	k_{IR}/θ_{IC}	$2k_{RI}/\theta_{RC}$	k_{IR}/θ_{IC}	k_{RI}/θ_{RC}	k_{IR}/θ_{IC}	-	-
$C^7 \leftrightarrow C^8$	$2k_{RI}/\theta_{RC}$	$2k_{IR}/\theta_{IC}$	k_{RI}/θ_{RC}	$2k_{IR}/\theta_{IC}$	-	-	-	-
$C^8 \leftrightarrow C^9$	k_{RI}/θ_{RC}	$3k_{IR}/\theta_{IC}$	-	-	-	-	-	-
$C^7 \leftrightarrow C^{10}$	k_{IA}/θ_{IC}	$2k_{AI}/\theta_{AC}$	k_{IA}/θ_{IC}	$2k_{AI}/\theta_{AC}$	k_{IA}/θ_{IC}	$2k_{AI}/\theta_{AC}$	-	-
$C^8 \leftrightarrow C^{11}$	$2k_{IA}/\theta_{IC}$	$2k_{AI}/\theta_{AC}$	$2k_{IA}/\theta_{IC}$	$2k_{AI}/\theta_{AC}$	-	-	-	-
$C^9 \leftrightarrow C^{12}$	$3k_{IA}/\theta_{IC}$	$2k_{AI}/\theta_{AC}$	-	-	-	-	-	-
$C^{10} \leftrightarrow C^{11}$	$2k_{RI}/\theta_{RC}$	k_{IR}/θ_{IC}	k_{RI}/θ_{RC}	k_{IR}/θ_{IC}	-	-	-	-
$C^{11} \leftrightarrow C^{12}$	k_{RI}/θ_{RC}	$2k_{IR}/\theta_{IC}$	-	-	-	-	-	-
$C^{11} \leftrightarrow C^{13}$	k_{IA}/θ_{IC}	$3k_{AI}/\theta_{AC}$	k_{IA}/θ_{IC}	$3k_{AI}/\theta_{AC}$	-	-	-	-
$C^{12} \leftrightarrow C^{14}$	$2k_{IA}/\theta_{IC}$	$3k_{AI}/\theta_{AC}$	-	-	-	-	-	-
$C^{13} \leftrightarrow C^{14}$	k_{RI}/θ_{RC}	k_{IR}/θ_{IC}	-	-	-	-	-	-
$C^{14} \leftrightarrow C^{15}$	k_{IA}/θ_{IC}	$4k_{AI}/\theta_{AC}$	-	-	-	-	-	-

Table S4. Transition rates between model open states.

# of activatable VSs	4		3		2		1	
	Forward	Reverse	Forward	Reverse	Forward	Reverse	Forward	Reverse
$O^1 \leftrightarrow O^2$	$4k_{RI}/\theta_{RO}$	k_{IR}/θ_{IO}	$3k_{RI}/\theta_{RO}$	k_{IR}/θ_{IO}	$2k_{RI}/\theta_{RO}$	k_{IR}/θ_{IO}	k_{RI}/θ_{RO}	k_{IR}/θ_{IO}
$O^2 \leftrightarrow O^3$	$3k_{RI}/\theta_{RO}$	$2k_{IR}/\theta_{IO}$	$2k_{RI}/\theta_{RO}$	$2k_{IR}/\theta_{IO}$	k_{RI}/θ_{RO}	$2k_{IR}/\theta_{IO}$	-	-
$O^3 \leftrightarrow O^4$	$2k_{RI}/\theta_{RO}$	$3k_{IR}/\theta_{IO}$	k_{RI}/θ_{RO}	$3k_{IR}/\theta_{IO}$	-	-	-	-
$O^4 \leftrightarrow O^5$	k_{RI}/θ_{RO}	$4k_{IR}/\theta_{IO}$	-	-	-	-	-	-
$O^2 \leftrightarrow O^6$	k_{IA}/θ_{IO}	k_{AI}/θ_{AO}	k_{IA}/θ_{IO}	k_{AI}/θ_{AO}	k_{IA}/θ_{IO}	k_{AI}/θ_{AO}	k_{IA}/θ_{IO}	k_{AI}/θ_{AO}
$O^3 \leftrightarrow O^7$	$2k_{IA}/\theta_{IO}$	k_{AI}/θ_{AO}	$2k_{IA}/\theta_{IO}$	k_{AI}/θ_{AO}	$2k_{IA}/\theta_{IO}$	k_{AI}/θ_{AO}	-	-
$O^4 \leftrightarrow O^8$	$3k_{IA}/\theta_{IO}$	k_{AI}/θ_{AO}	$3k_{IA}/\theta_{IO}$	k_{AI}/θ_{AO}	-	-	-	-
$O^5 \leftrightarrow O^9$	$4k_{IA}/\theta_{IO}$	k_{AI}/θ_{AO}	-	-	-	-	-	-
$O^6 \leftrightarrow O^7$	$3k_{RI}/\theta_{RO}$	k_{IR}/θ_{IO}	$2k_{RI}/\theta_{RO}$	k_{IR}/θ_{IO}	k_{RI}/θ_{RO}	k_{IR}/θ_{IO}	-	-
$O^7 \leftrightarrow O^8$	$2k_{RI}/\theta_{RO}$	$2k_{IR}/\theta_{IO}$	k_{RI}/θ_{RO}	$2k_{IR}/\theta_{IO}$	-	-	-	-
$O^8 \leftrightarrow O^9$	k_{RI}/θ_{RO}	$3k_{IR}/\theta_{IO}$	-	-	-	-	-	-
$O^7 \leftrightarrow O^{10}$	k_{IA}/θ_{IO}	$2k_{AI}/\theta_{AO}$	k_{IA}/θ_{IO}	$2k_{AI}/\theta_{AO}$	k_{IA}/θ_{IO}	$2k_{AI}/\theta_{AO}$	-	-
$O^8 \leftrightarrow O^{11}$	$2k_{IA}/\theta_{IO}$	$2k_{AI}/\theta_{AO}$	$2k_{IA}/\theta_{IO}$	$2k_{AI}/\theta_{AO}$	-	-	-	-
$O^9 \leftrightarrow O^{12}$	$3k_{IA}/\theta_{IO}$	$2k_{AI}/\theta_{AO}$	-	-	-	-	-	-
$O^{10} \leftrightarrow O^{11}$	$2k_{RI}/\theta_{RO}$	k_{IR}/θ_{IO}	k_{RI}/θ_{RO}	k_{IR}/θ_{IO}	-	-	-	-
$O^{11} \leftrightarrow O^{12}$	k_{RI}/θ_{RO}	$2k_{IR}/\theta_{IO}$	-	-	-	-	-	-
$O^{11} \leftrightarrow O^{13}$	k_{IA}/θ_{IO}	$3k_{AI}/\theta_{AO}$	k_{IA}/θ_{IO}	$3k_{AI}/\theta_{AO}$	-	-	-	-
$O^{12} \leftrightarrow O^{14}$	$2k_{IA}/\theta_{IO}$	$3k_{AI}/\theta_{AO}$	-	-	-	-	-	-
$O^{13} \leftrightarrow O^{14}$	k_{RI}/θ_{RO}	k_{IR}/θ_{IO}	-	-	-	-	-	-
$O^{14} \leftrightarrow O^{15}$	k_{IA}/θ_{IO}	$4k_{AI}/\theta_{AO}$	-	-	-	-	-	-
$C^n \rightarrow O^n$	$k_{CO}/(\theta_{RC}^{n(R)} * \theta_{IC}^{n(I)} * \theta_{AC}^{n(A)})$							
$O^n \rightarrow C^n$	$k_{OC}/(\theta_{RO}^{n(R)} * \theta_{IO}^{n(I)} * \theta_{AO}^{n(A)})$							

Supplementary References

1. Murray CI*, et al.* (2016) Unnatural amino acid photo-crosslinking of the IKs channel complex demonstrates a KCNE1:KCNQ1 stoichiometry of up to 4:4. *eLife* 5:1-18.
2. Westhoff M, Murray CI, Eldstrom J, & Fedida D (2017) Photo-Cross-Linking of I. *Biophys J* 113(2):415-425.
3. Thompson E*, et al.* (2017) cAMP-dependent regulation of IKs single-channel kinetics. *J Gen Physiol* 149(8):781-798.
4. Werry D, Eldstrom J, Wang Z, & Fedida D (2013) Single-channel basis for the slow activation of the repolarizing cardiac potassium current, I(Ks). *Proc Natl Acad Sci USA* 110(11):E996-1005.
5. Eldstrom J, Wang Z, Werry D, Wong N, & Fedida D (2015) Microscopic mechanisms for long QT syndrome type 1 revealed by single-channel analysis of IKs with S3 domain mutations in KCNQ1. *Heart Rhythm* 12(2):386-394.
6. Es-Salah-Lamoureux Z, Fougere R, Xiong PY, Robertson GA, & Fedida D (2010) Fluorescence-tracking of activation gating in human ERG channels reveals rapid S4 movement and slow pore opening. *PLoS One* 5(5):e10876.
7. Santiago-Castillo JA, Covarrubias M, Sánchez-Rodríguez JE, Perez-Cornejo P, & Arreola J (2010) Simulating complex ion channel kinetics with IonChannelLab. *Channels (Austin)* 4(5):422-428.
8. Colquhoun D & Hawkes AG (1995) A Q-matrix cookbook: how to write only one program to calculate the single-channel and macroscopic predictions for any kinetic mechanism. *Single-Channel Recording*, eds Sakmann B & Neher E (Springer), 2nd Ed, pp 589-633.
9. Zaydman MA*, et al.* (2014) Domain-domain interactions determine the gating, permeation, pharmacology, and subunit modulation of the IKs ion channel. *Elife.* 3:e03606.